CARBON 74 (2014) 54–62

Available at www.sciencedirect.com

ScienceDirect

journal homepage: www.elsevier.com/locate/carbon

Shear effects on expanded graphite under uniaxial pressure: An *in situ* small angle neutron scattering study

Félix Balima [a,*], *Sylvie Le Floch* [a], *Alfonso San-Miguel* [a], *Peter Lindner* [b], *Annie Brûlet* [c], *Laurent Duclaux* [d], *Vittoria Pischedda* [a,*]

[a] *Institut Lumière Matière, UMR5306 Université Lyon 1-CNRS, Université de Lyon, 69622 Villeurbanne Cedex, France*
[b] *Institut Max von Laue–Paul Langevin, 38042 Grenoble Cedex, France*
[c] *Laboratoire Léon Brillouin, UMR12 CEA-CNRS, CEA-Saclay, 91191 Gif-sur-Yvette Cedex, France*
[d] *LCME, Université de Savoie, 73376 Le Bourget du Lac Cedex, France*

ARTICLE INFO

Article history:
Received 22 November 2013
Accepted 1 March 2014
Available online 6 March 2014

ABSTRACT

In a previous work [1] we elucidated the *in situ* evolution of the porosity of *out-of-plane* compressed flexible graphite under uniaxial pressure up to 1000 bar using small-angle neutron scattering (SANS) technique. In order to understand the influence of shear effect on the properties of flexible graphite we study, in the present paper, the *in situ* behaviour of *in-plane* compressed flexible graphite under a uniaxial pressure. The sample had a pleated layered structure in which anisotropic SANS patterns revealed a distribution of differently oriented ellipsoid pores. Uniaxial compression generates important shear effects in this kind of sample.

We have determined the evolution of the system fractal dimension, pore size distribution and apparent specific surface area with applied pressure which together allow us to describe the meso and macro pore structure evolution. Under pressure, the irreversible collapse and splitting of larger pores into smaller size ones which is characteristic of *out-of-plane* uniaxial compression [1], is accompanied, in the presence of shear stress components, by an *in-plane* slipping mechanism giving rise to cracks and consequently to interface formation.

1. Introduction

Compressed expanded graphite, known as flexible graphite, is obtained by compressing exfoliated graphite flakes without a binder. The resulting flexible graphite is an anisotropic system with high porosity (around 60%). It is used as sealing gasket, heating element, adsorbent, lubricant or electrochemical support in a wide range of applications in industries as diverse as nuclear power, petrochemicals or pharmaceuticals [2–5] due to properties such as resilience, high compressibility and elastic recovery, as well as chemical resistance and good thermal and electrical conduction in the *in-plane* direction. These properties are affected by the introduction of meso and macro porosity in the material through exfoliation and densification processes.

In a large range of industrial uses (sealing, damping or absorption in pressurized media), flexible graphite is used under varied conditions of static and dynamic pressure or

* *Corresponding authors:* Fax: +33 472432648.
E-mail addresses: felix.balima@univ-lyon1.fr (F. Balima), vittoria.pischedda@univ-lyon1.fr (V. Pischedda).
http://dx.doi.org/10.1016/j.carbon.2014.03.002
0008-6223/

stress. Understanding the influence of meso and macro pore structure on macroscopic behaviour under working conditions is therefore essential to improve function and surpass the current application limits.

The link between porosity and macroscopic features such as permeability, mechanical or electrochemical properties has been investigated for several porous materials [6–8]. In particular, the influence of manufacturing stresses on the density and mechanical properties of flexible graphite has been studied [9–11]. In a recent work [1], we have elucidated the evolution of the meso and macro pore structure as a function of the working stress conditions up to 1000 bar for *out-of-plane* compressed flexible graphite through an *in situ* small angle neutron scattering (SANS) experiment. The compressive force was applied perpendicular to the flexible graphite sheets and parallel to the average c-axis of the graphite crystallites. The meso and macro pore evolution under uniaxial pressure was studied using fractal dimension and specific area as key parameters. We observed that larger pores irreversibly collapsed and split into smaller size ones under uniaxial pressure.

For many applications such as sealing and vibration damping, flexible graphite is manufactured using an *in-plane* compression (parallel to the flexible sheet longitudinal direction). The resulting flexible graphite has a quite complex texture (described later in the manuscript) that improves the elastic recovery and vibration absorption. The present paper aims to investigate, by an *in situ* small angle neutron scattering method, the porosity evolution of *in-plane* compressed flexible graphite. From the pressure dependence of the different extractable parameters (fractal dimension, porosity and apparent specific surface area), we intend to understand how the evolution of porosity with pressure determines the mechanical behaviour of compressed flexible graphite under working conditions.

2. Experimental

2.1. Sample description

We studied a Die-formed Flexible Graphite (DFG) sample (Fig. 1) which is normally used as sealing gasket and was provided by Technetics Group (Saint Etienne, France). DFG is manufactured from parallel flexible graphite ribbons pressed in a mould. The manufacturing pressure (P_M) was applied parallel to the sheet longitudinal direction (*in-plane* compression) (Fig. 1a). This yields to the pleating of the flexible graphite sheets as shown in Fig. 1c. In the DFG sample, the dominant orientation of the c-axis of the crystallites is still perpendicular to the direction of P_M.

The DFG sample had a thickness $t = 5$ mm, length $\ell = 23$ mm and height $h = 15$ mm (Fig. 1b). The total porosity of the DFG sample evaluated from the measured apparent density of 1.54 g cm^{-3} is around 31%, deduced from the graphite skeletal density of 2.23 g cm^{-3}. As the X-ray diffraction signature of our sample is similar to that of bulk graphite, this assumption is valid (Supplementary Fig. S1). To perform SANS high pressure experiments the DFG sample was placed in an in-house designed pressure cell [1,12]. The pressure was applied along the direction of e_z to simulate the working conditions of a sealing gasket.

2.2. Small angle neutron scattering

The SANS experiments were performed on two different beamlines: (a) the D11 beamline at ILL (Institut Laue Langevin) neutron source (Grenoble, France) using a 4.51 Å wavelength, 5 mm diameter beam size and a ^{3}He detector and (b) the PAXE beamline at LLB (Laboratoire Léon Brillouin) neutron source (Saclay, France) using a 6 Å wavelength, 7 mm diameter beam size and a BF_3 detector. On the D11 instrument, we used three sample-detector distances of 1.8, 8 and 39 m to cover a q-range of $2.5 * 10^{-3}$–0.5 Å^{-1} while two sample-detector distances were used on the PAXE beamline to cover a q-range of $6.5 * 10^{-3}$–0.35 Å^{-1}.

The raw scattering intensities were corrected to account for empty cell scattering, sample transmission as well as sample thickness following classical SANS data analysis procedures [13]. Differential cross sections per unit sample volume (cm^{-1} units) were obtained using precalibrated secondary standards (water at D11 and plexiglass at PAXE) and direct determination of incident neutron beam flux.

The $t = 5$ mm sample was maintained by two 4 mm thick single crystal sapphire windows to avoid any extrusion. These transparent windows allow an irradiation surface area with the neutron beam of 78 mm^2.

The pressure was increased stepwise up to the maximum pressure of 1000 bar and decreased stepwise back to ambient pressure. The SANS spectra were collected *in situ* at each 200 bar step.

Integrated data were obtained from the raw data using ILL's standard SANS software [14] and the LLB in-house software PAsiNET [15]. As the obtained patterns were elliptic, the intensity was integrated along the two axis directions of these elliptic patterns in a 30° width circular sector around each axis (shaded sectors in Fig. 2), following a common method for data analysis [1,16,17]. These two axes were parallel and perpendicular to the working pressure P_W direction (Fig. 2).

Specific fitting scripts were written to extract the fractal dimension and the correlation length from each of the two 30° integrated sections. To calculate the apparent specific surface area from the apparent Porod's constant using the Hurd formula [18] we integrated the 30° circular sectors in steps of 30° to complete the 360° around the beam centre.

3. Results and discussion

All the collected SANS patterns were elliptic (Fig. 2) suggesting the non-spherical shape of the scatterers. Henceforth, $I_{//}(q)$ and $I_{\perp}(q)$ are the scattered intensities in the direction parallel and perpendicular to the applied uniaxial pressure respectively.

In the previously studied *out-of-plane* compressed flexible graphite [1], the oblate spheroidal pores had their equatorial plane perpendicular to the applied pressure direction. In the current DFG sample, the equatorial plane of this pore model volume is distorted under the *in-plane* manufacturing

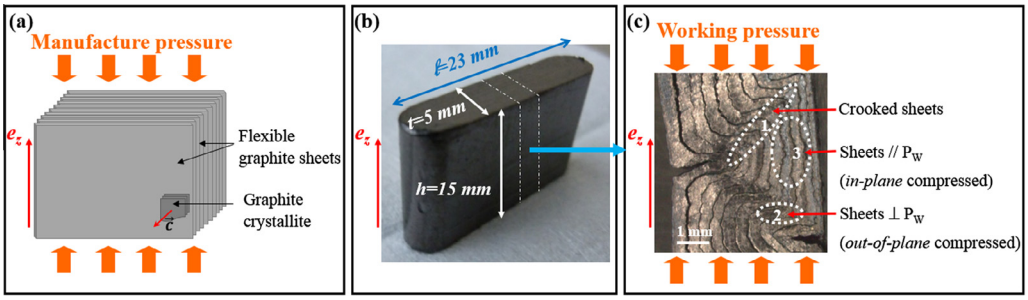

Fig. 1 – (a) Schematic view of the die-formed flexible graphite (DFG) manufacturing process. The manufacturing compressive force, following the direction of e_z, was parallel to the average flexible graphite sheet longitudinal direction, perpendicular to the average c-axis of the graphite crystallites. (b) DFG sample photograph with dimensions. (c) Magnified longitudinal view of a slice of DFG sample where we can observe: (1) crooked, (2) *out-of-plane* and (3) *in-plane* compressed flexible graphite sheets. The slice was cut from the sample as indicated by the dashed lines on panel (b). The intersheet spaces were formed during the cutting process. (A colour version of this figure can be viewed online.)

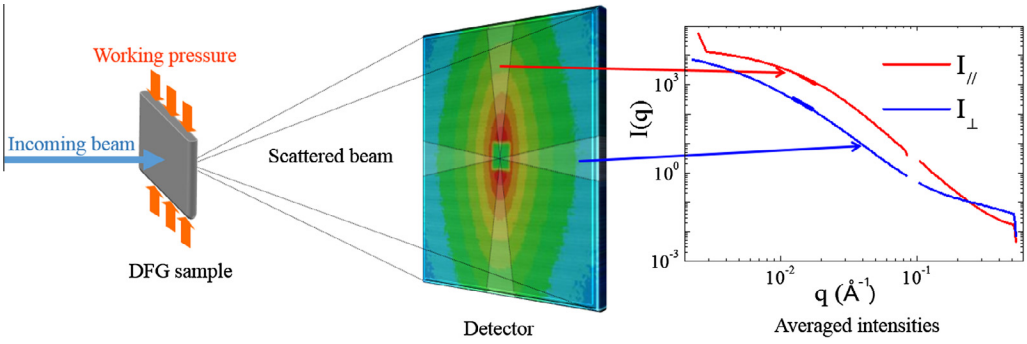

Fig. 2 – Scheme of our high pressure SANS experimental setup. The scattered beam was collected on the ^{3}He detector of D11. The elliptical pattern was averaged following directions parallel and perpendicular to the applied pressure (i.e. the working pressure) indicated by the orange arrows. Shaded sectors on the pattern indicate the 30° angular sectors used to obtain the integrated intensities $I_{//}(q)$ and $I_{\perp}(q)$. The corresponding averaged intensities are shown on the right. (A colour version of this figure can be viewed online.)

compression (Fig. 3a). To investigate the resulting distorted pore shape, we collected patterns from an individual flexible graphite sheet cleaved from the DFG sample, the incoming beam being normal to the sheet. The pattern thus obtained was elliptical. By contrast, such an experimental configuration gave an isotropic pattern for the *out-of-plane* compressed flexible graphite studied in Ref. [1]. As there was no indication of any symmetry axis, the average pore shape model was assumed to be an ellipsoid with three distinct axes: the e_x long axis and both e_y and e_z short axes ($e_y \neq e_z$) (Fig. 3b).

Fig. 4 shows the evolution of selected scattered intensity versus q along the directions parallel and perpendicular to P_W axis.

For the *in situ* high pressure SANS acquisitions the sample thickness was t = 5 mm imposed by the compression chamber geometry. For this t = 5 mm sample, the low neutron transmission value (in the range of 0.28–0.35 from ambient pressure to 1000 bar) indicates the possible presence of multiple scattering (MS). The effect of MS is characterized by a broadening of the scattering profile. By varying the sample thickness or the incoming beam wavelength, scattering distortions characteristic of MS might be detected. To investigate the MS occurrence the procedure detailed in Ref. [1] was used. Fig. 5 shows data collected on PAXE at ambient conditions with a t = 2.4 mm sample obtained by cutting the t = 5 mm pristine sample. Additional data collected using two different wavelengths (Supplementary Fig. S2) show that MS affects our data in the region below 3×10^{-2} Å^{-1} where the scattered intensity of the thicker t = 5 mm sample (Fig. 5) decreases. However, MS effects do not modify the slope of the linear domain from where the value of the fractal dimension is obtained [19–21].

The linear domain extension range depends on the scattering direction. Using the 4.5 Å wavelength beam at D11 we obtained 1.3 and 1 order of magnitude for $I_{//}(q)$ and for $I_{\perp}(q)$ respectively. For a thinner sample, the MS is reduced, so the linear domain extends for a higher q domain. The fractal nature of our DFG sample is then confirmed.

To extract information on the average pore shape in the sample at ambient conditions, we used the low q-domain of the 2.4 mm thick sample which is less affected by MS. For a random two-phase system, the Debye model allows extracting the correlation length ξ in the low q range. Obviously, our system is not random. However, we could use this model by introducing different correlation lengths along each of the two axes of the elliptic pattern [22], corresponding to the e_x and e_z axes of the pore ellipsoid (Fig. 3). The scattered

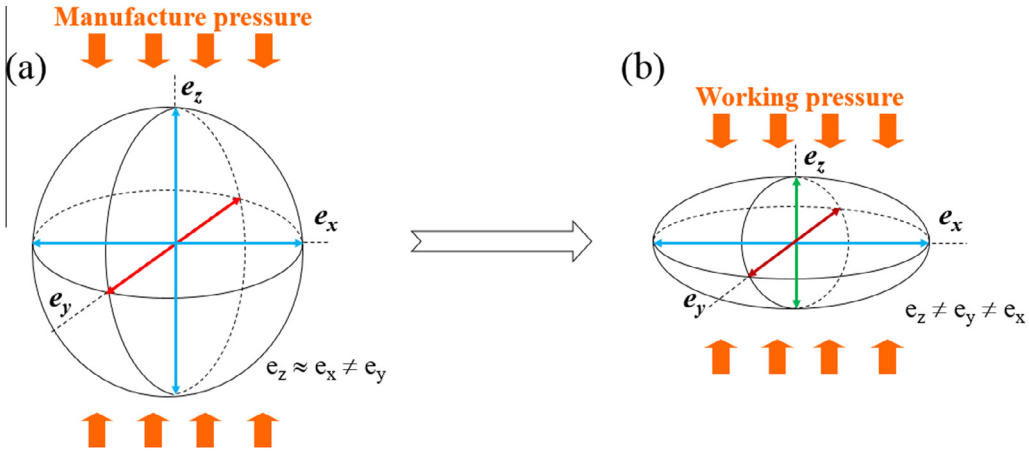

Fig. 3 – Pore morphology in the compressed flexible graphite. The spheroidal pore shape (a) observed for the out-of-plane compressed flexible graphite [1] was transformed to an ellipsoïdal shape (b) by the manufacture pressure (P_M). P_M as well as working pressure (P_W) were applied following the direction of e_z. The incoming neutron beam in our high pressure experiments is parallel to the e_y direction. (A colour version of this figure can be viewed online.)

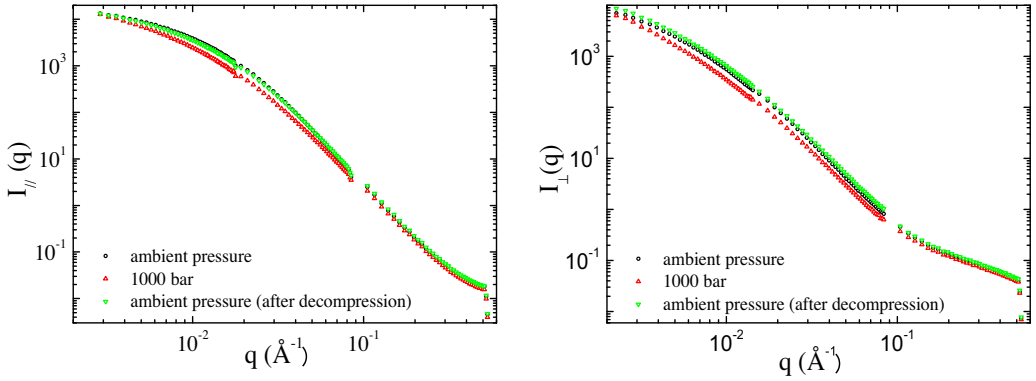

Fig. 4 – SANS scattered intensity versus q along axes parallel and perpendicular to the applied pressure for DFG sample at different pressure conditions. Patterns were taken on the D11 instrument at ILL with a 4.5 Å wavelength neutron beam. (A colour version of this figure can be viewed online.)

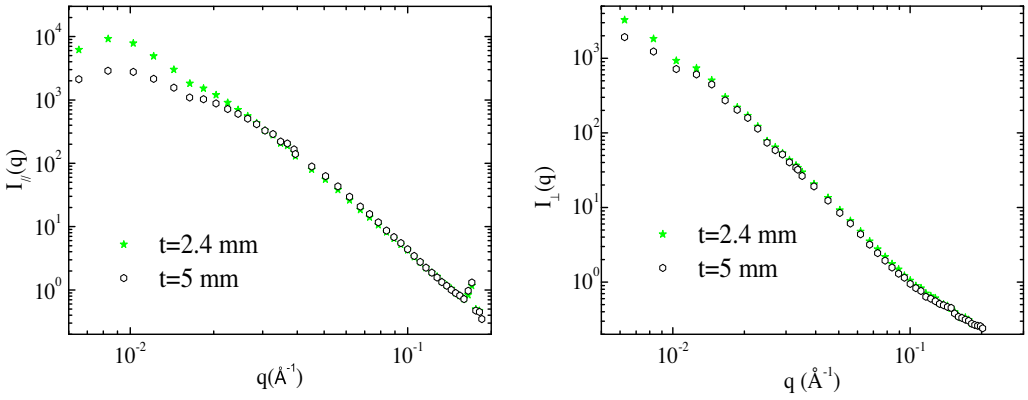

Fig. 5 – SANS intensity versus q plot at ambient pressure for two different DFG sample thicknesses collected at 6 Å wavelength (LLB) parallel (left) and perpendicular (right) to the applied uniaxial pressure. Spectra were rescaled to superimpose the linear domains. (A colour version of this figure can be viewed online.)

intensities $I_{//}(q)$ and $I_{\perp}(q)$ were fitted by the equation $I(q) = I_0/(1 + q^2\xi^2)^2$.

From the linear slope of $I(q)^{-1/2}$ versus q^2 plot (Supplementary Fig. S3), the correlation length was estimated to be

70 ± 5 Å and 105 ± 7 Å for $I_{//}(q)$ and $I_{\perp}(q)$ respectively. These values support an ellipsoidal pore model.

The validity of the fractal model in this type of sample was discussed in detail in Ref. [1]. In the high q region, the scattered intensity $I(q)$ follows a power law $I(q)_{q\to\infty} \propto q^{d-6}$, where d is the fractal dimension of the system. This fractal dimension is obtained in a limited q domain corresponding to pore sizes 4 Å < r < 250 Å, calculated from $r = 2.5/q$, as used for surface fractal systems [23]. For a perfectly smooth surface $d = 2$, while $d = 3$ for a rough surface sufficiently convoluted to fill a 3D volume.

Fig. 6 shows the evolution of fractal dimension along the two directions parallel ($d_{//}$) and perpendicular ($d_{\perp}$) to the applied pressure direction during compression up to 1000 bar and decompression. We observe an important fractal anisotropy which is preserved under pressure: $d_{//}$, the fractal dimension extracted from $I_{//}(q)$, has lower values than $d_{\perp}$, the fractal dimension extracted from $I_{\perp}(q)$.

The fractal dimension increases continuously during compression up to a maximum value depending on direction. During the decompression steps the fractal dimension decreases and the recovery is partial. Fundamentally, the higher the surface fractal dimension the rougher the interface between the pore and graphite matrix [24,25]. In our experiment, the densification of the samples is probably associated with space vanishing and increasing pore–matrix interface roughness.

The evolution of total porosity under pressure (Fig. 7) was obtained from the sample volume variation (calculated from the piston displacement) under compression and decompression. The loss of total porosity is about 32% at 1000 bar and 25% after decompression. This pressure-dependence of porosity is almost not observed in the pore size distribution (PSD) evolution extracted from SANS data. To extract the PSD (also known as pore number density) in the high linear

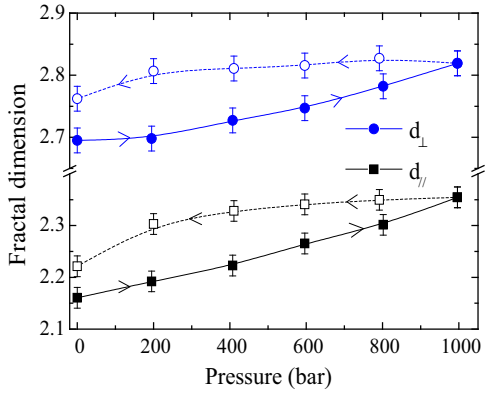

Fig. 6 – Evolution of the fractal dimension as a function of the applied uniaxial pressure for the DFG sample. For each compression and decompression step, the fractal dimension was calculated from the scattered intensity curves along the two directions parallel ($d_{//}$) and perpendicular ($d_{\perp}$) to the applied pressure direction. Filled symbols stand for the compression and empty symbols for the decompression. Lines are visual guides. (A colour version of this figure can be viewed online.)

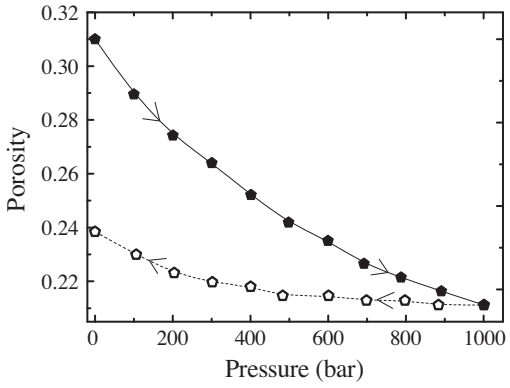

Fig. 7 – Total porosity evolution calculated from the sample volume variation with applied pressure (initial porosity: 31%). Filled symbols stand for compression and empty symbols for decompression.

q region ($q > 0.0125$ Å^{-1}) of $I_{\perp}$, unaffected by the MS, we used the polydisperse sphere model in PRINSAS software [26]. We observed that PSD does not vary within the error bars after applying on the sample a pressure of 1000 bar and after decompression. This indicates that the small size pore fraction along the direction perpendicular to P_W (axis e_z in Fig. 3) is not pressure sensitive and that the decrease of total porosity under compression observed in Fig. 7 is due to the pore size range larger than ~250 Å.

Let us consider the evolution of the specific surface area under pressure which is proportional to the asymptotic value of $I(q)q^{(6-d)}$ [18]. The specific surface area A of a surface fractal, scaled with a length scale r_0 is given by:

$$A = Sr_0^{2-d}$$

where d is the fractal dimension of the system. S is calculated from the intensity curve in the high q region:

$$S = \frac{\lim_{q\to\infty} I(q)q^{(6-d)}}{\pi(\Delta\rho)^2\eta F(d)}$$

where $\Delta\rho$ is the scattering length density contrast, η is the sample density and $F(d)$ is a function of the fractal dimension given by [27]:

$$F(d) = \frac{\Gamma(5-d)\sin[(3-d)\pi/2]}{(3-d)}$$

The specific surface area had an anisotropic distribution. We thus calculated the apparent specific surface area in different directions using the scattered intensity curves and a $r_0 = 2.58$ Å length scale corresponding to the radius of krypton atom [18]. The calculated apparent specific area along the directions parallel and perpendicular to the direction of P_W are called $AS_{//}$ and $AS_{\perp}$. Fig. 8 shows the evolution of $AS_{//}$ and $AS_{\perp}$ with the working pressure.$AS_{//}$ slightly increases under compression while $AS_{\perp}$ decreases. Under decompression, both $AS_{\perp}$ and $AS_{//}$ increase with respect to the high pressure values. The apparent specific surface area increase is related to a pore–matrix interface formation. Surprisingly, during decompression, a new pore–matrix interface is generated mostly along the uniaxial pressure direction as $AS_{//}$ increases. The apparent specific area evolution is different from what

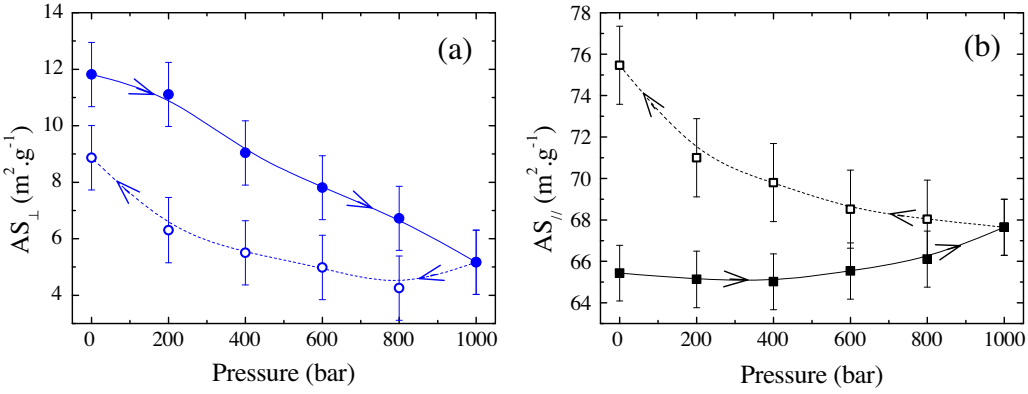

Fig. 8 – Evolution of the apparent specific surface area of the DFG sample at ambient pressure, 1000 bar, and after decompression. Symbols correspond to the calculated values of the apparent specific area at each 30° sector around the beam centre deduced from scattering curves (Fig. 4) by using the asymptotic value of $I(q)q^{(6-d)}$. Spline lines are guides for eyes. $AS_{//}$ and $AS_{\perp}$ correspond to the apparent specific area along the parallel and perpendicular directions relative to the P_W. (A colour version of this figure can be viewed online.)

was observed for the *out-of-plane* compressed graphite [1] where the apparent specific area had an irreversible increase perpendicularly to the applied pressure direction and an almost irreversible decrease in the parallel direction. This behaviour was attributed to interface creation induced by the irreversible collapse and splitting of larger pores into smaller ones [1]. As seen in Fig. 1c, in the DFG sample the flexible graphite sheets have not a unique preferential orientation. Consequently, the induced pore orientation is also complex and gives a mean pore shape shown in Fig. 3. As seen in our prior work [1] and reminded in Section 2.1, the average pore is oriented with its long axis perpendicular to the *c*-axis of the graphite crystallites.

Combining our results, we tried to rationalize the pore evolution of the DFG sample under a uniaxial load. First we have to consider the different pore orientations in the pleated sample described in Fig. 1c. The dynamic mechanical behaviour of flexible graphite has been recently studied by Chen and Chung [11] in a non-confined environment. Compression tests were made on three different specimens with flexible graphite sheet configurations close to the ones observed in our DFG sample and described in Fig. 1c: (1) *crooked*, (2) *out-of-plane* and (3) *in-plane* compressed flexible graphite sheets.

Let us now analyse the evolution of each of these three regions under uniaxial pressure and the consequences on the SANS signal.

Region 1. Crooked. Under compression the crooked section of flexible graphite is subjected to shear stresses. As it has been already observed this brings to displacement of crystallites [11] that eventually results in crack formation. It has been shown that for high density flexible graphite sheets the resistance to motion and friction between interlocked micro-disc-shaped graphite sheets can cause the fracture of disks [28]. From a morphological point of view the pores flatten [11] and their aspect ratio increases. This region in the sample would then likely contribute to create under compression new interface in both directions parallel and perpendicular to the direction of P_W.

Region 2. Out-of-plane. In the *out-of-plane* compression the pressure axis e_z is parallel to the *c*-axis of the graphite crystallites (Fig. 1c). This corresponds to the same configuration observed in our previous study of an *out-of-plane* flexible graphite [1], in which the uniaxial pressure was applied perpendicular to the average spheroidal pore long axis. In the DFG sample the pores were flattened during the manufacturing process and have an average ellipsoidal shape as explained above (Fig. 3). Within the approximation that the *in-plane* manufacturing compression did not change the flexible graphite properties, we can apply, for this region of the DFG, the same pore collapse model described in our previous work [1]. Under compression, the pores undergo an irreversible collapse and splitting into smaller size ones, concomitant to the formation of a new pore interface along the direction perpendicular to P_W. This would correspond to an irreversible increase of $AS_{\perp}$ after decompression [1].

Region 3. In-plane. Let us consider now the last and most predominant case, where the flexible graphite sheets are parallel to the direction of the applied pressure: the *in-plane* compression (Fig. 1c). In lamellar compounds submitted to shear stress, the crystallite slipping mechanism has been the key phenomenon [11,29,30] to understand their mechanical behaviour. The defects in such materials facilitate a shear response to compression, tension or flexion [30–32]. In our highly disordered graphite, there is a considerable amount of potential shear starting points. At the nanoscale, the crystallite edges can be considered as defects. As for the crooked region, the applied pressure would likely cause a relative motion of the crystallites along the direction of e_z (which is the applied pressure direction) and the overlapping of the edges. During the experiment, after increasing the hydraulic pressure in the cell pump system, we had to wait for a satisfactory pressure stabilisation time to reach equilibrium. This pressure relaxation time could be due to the *in-plane* slipping mechanism of the crystallites.

Local frictions may cause also wrinkles, buckling, splitting or cleavage of the crystallites which are crack formation fac-

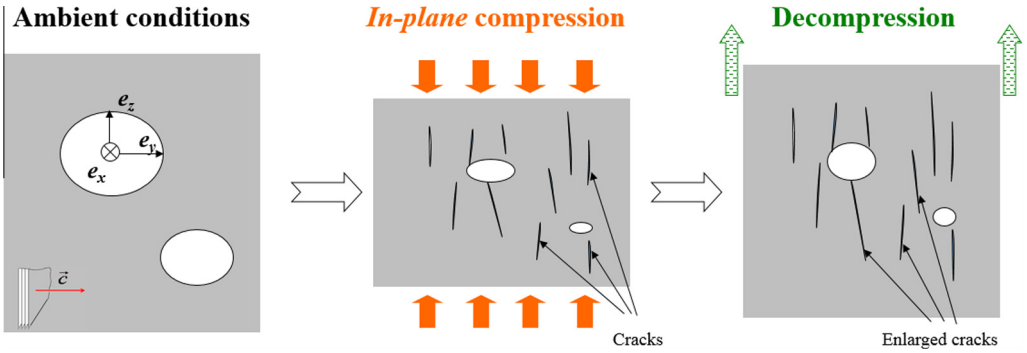

Fig. 9 – Schematic side view of pores (with a magnified scale) in the DFG sample under compression and decompression. The average crystallographic c-axis of crystallites is shown on the left bottom side. The ellipsoid pore is cut in the plane containing e_z and e_y axes (see also Fig. 3). The pore long axis e_x is perpendicular to the average crystallite c-axis. We propose a model where cracks arise and propagate from largest pores within the graphite matrix as a shear response of crystallites to the compression. Under decompression we observe a partial sample elastic recovery involving crack and pore elongation. (A colour version of this figure can be viewed online.)

tors. It was stated previously that cracks should start from the largest pores [29]. Crack occurrence presumes interface creation in agreement with the observed increase of the apparent specific area, $AS_{//}$, along the e_z direction during the decompression. Due to the elastic behaviour of DFG sample, the pressure release enlarges the crack dimension along the direction of e_z. In Fig. 9, we propose a schematic view of the pore evolution under compression and decompression consistent with the observed parameters (fractal dimension and apparent specific area) evolution. Under compression, the slipping and fracture of the crystallites would create pore-matrix interface. During decompression, the created cracks would enlarge due to the released of accumulated energy from residual stress and likely induce an increase in the apparent specific surface area, mostly along P_W direction.

The fact that the sample was confined in the compression chamber of the pressure cell means that only its height (in the direction of e_z) could change under compression. Confinement stresses (in the e_xe_y plane), due to the rigid walls of the compression chamber, contribute to keep the crystallites aligned along the direction of e_z during the compression. The decompression was followed by a significant recovery of the sample volume due to the well-known elastic behaviour of flexible graphite [29] and the enlargement of cracks along the direction of e_z. This is confirmed by $AS_{//}$ increase after decompression.

Porosity measurement by mercury intrusion was performed on our DFG samples before and after the pressure cycle (Fig. 10). Mercury intrusion, which assumes a cylindrical pore morphology, allows probing the open porosity. It revealed two populations of pores in both samples: mesopores with a mean pore diameter of about 25 nm and macropores larger than 50 μm. The main modification induced by the pressure cycle is the increase in the open macropore volume. This result is in agreement with the proposed scenario of cracks formation due to the shear stress induced in the graphite matrix by compression.

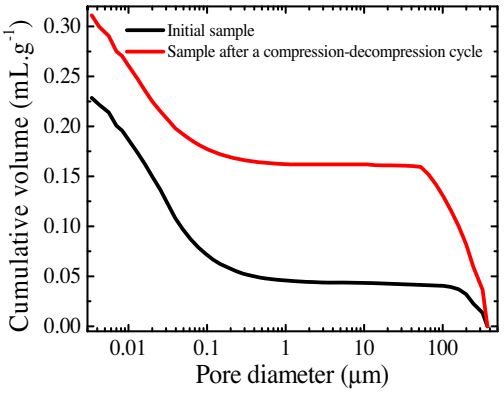

Fig. 10 – Mercury intrusion porosimetry curves for the initial DFG (black) and for the same sample decompressed from 1000 bar (red). (A colour version of this figure can be viewed online.)

4. Conclusion

The evolution of porosity of die-formed flexible graphite was investigated *in situ* under uniaxial pressure up to 1000 bar using SANS. The initial sample had a pleated layer structure. The anisotropy of the accessible parameters revealed an anisotropic pore shape which was assumed to be ellipsoidal to fit the SANS data. Analysis of the data yielded the fractal dimension, average pore size distribution, total porosity and apparent specific surface area, along the two directions parallel and perpendicular to the compression direction P_W.

After a pressure cycle (up to 1000 bar and back to ambient pressure), we observed: (a) an irreversible decrease in porosity; (b) an irreversible increase in the apparent specific surface area and fractal dimension along the compression direction, P_W. This, we interpret, is related to the pore volume reduction accompanied by crack formation and consequently to new pore–matrix interface creation. The evolution of the SANS signal under pressure showed that the system response to the mechanical load is strongly affected by the shear forces acting along the direction of P_W.

During decompression, we observed a partial elastic recovery involving some crack elongation along the direction of P_W. The crack creation was confirmed by mercury intrusion measurements on a sample after a cycle of compression-decompression.

Simultaneously to this predominant shear effect, the pore collapse and splitting mechanism described in Ref. [1] also acts in the *out-of-plane* compressed region of the sample.

This study, in which the shear component is relevant, is in contrast with our previous work on *out-of-plane* compressed flexible graphite for which shear effects were negligible. Together, our present work and Ref. [1] provide an accurate understanding of the evolution of porosity and the pore–matrix interface of flexible graphite when submitted to mechanical compression.

This type of high pressure *in situ* study could be applied to other porous lamellar systems to obtain a complete description of the evolution with mechanical constraints of these systems, important both for natural and applied sciences.

Acknowledgements

This research was supported by the "Agence Nationale de la Recherche" (ANR) through MATETPRO project ANR-08-MAPR-0011. We are indebted to Prof. Andrzej Radlinski (*Griffith University*, Australia) for his kind help with data processing using PRINSAS and useful discussion. We would like to thank Technetics Group France for providing samples, Hervé Feret for his technical assistance in the pressure cell development, Dr. Laurent Gremillard (INSA-Lyon, France) for porosity measurements by mercury intrusion and David Bowyer for technical assistance during the experiment on the D11 beamline at ILL (Grenoble, France).

Appendix A. Supplementary data

Supplementary data associated with this article can be found, in the online version, at http://dx.doi.org/10.1016/j.carbon.2014.03.002.

REFERENCES

[1] Balima F, Pischedda V, Le Floch S, Brûlet A, Lindner P, Duclaux L, et al. An in situ small angle neutron scattering study of expanded graphite under a uniaxial stress. Carbon 2013;57:460–9.
[2] Celzard A, Marêché JF, Furdin G. Modelling of exfoliated graphite. Prog Mater Sci 2005;50:93–179.
[3] Rouquerol J, Avnir D, Fairbridge C, Everett D, Haynes J, Pernicone N, et al. Recommendations for the characterization of porous solids. Pure Appl Chem 1994;66:1739–58.
[4] Chung DDL. Exfoliation of graphite. J Mater Sci 1987;22:4190–8.
[5] Biloé S, Mauran S. Gas flow through highly porous graphite matrices. Carbon 2003;41:525–37.
[6] Xu P, Yu B. Developing a new form of permeability and Kozeny–Carman constant for homogeneous porous media by means of fractal geometry. Adv Water Resour 2008;31:74–81.
[7] Ruffet C, Gueguen Y, Darot M. Complex conductivity measurements and fractal nature of porosity. Geophysics 1991;56:758–68.
[8] Tian Y, Song Y, Tang Z, Guo Q, Liu L. Influence of high temperature treatment of porous carbon on the electrochemical performance in supercapacitor. J Power Sources 2008;184:675–81.
[9] Dowell MB, Howard RA. Tensile and compressive properties of flexible graphite foils. Carbon 1986;24:311–23.
[10] Gu J, Leng Y, Gao Y, Liu H, Kang F, Shen W. Fracture mechanism of flexible graphite sheets. Carbon 2002;40:2169–76.
[11] Chen P-H, Chung DDL. Dynamic mechanical behavior of flexible graphite made from exfoliated graphite. Carbon 2012;50:283–9.
[12] Balima F, Pischedda V, Le Floch S, San-Miguel A. High pressure small angle scattering study of porous lamellar systems: the case of expanded vermiculite and expanded graphite. France: Biarritz; 2010.
[13] Cotton J-P. Introduction to scattering experiments. Neutrons X-Rays Light Scatt. Methods, Amsterdam: Elsevier; 1991, p. 1–31.
[14] Ghosh R, Egelhaaf S, Rennie A. A computing guide for small-angle scattering experiments. Grenoble, France: Institut Laue Langevin; 2006.
[15] Brûlet A, Lairez D, Lapp A, Cotton J-P. Improvement of data treatment in small-angle neutron scattering. J Appl Crystallogr 2007;40:165–77.
[16] Radlinski AP, Mastalerz M, Hinde AL, Hainbuchner M, Rauch H, Baron M, et al. Application of SAXS and SANS in evaluation of porosity, pore size distribution and surface area of coal. Int J Coal Geol 2004;59:245–71.
[17] Keller T, Wagner W, Margadant N, Siegmann S, Ilavský J, Písačka J. Characterization of anisotropic, thermally sprayed microstructures using small-angle neutron scattering. Brno: Czech Republic; 2001. p. 460–8.
[18] Hurd AJ, Schaefer DW, Smith DM, Ross SB, Le Méhauté A, Spooner S. Surface areas of fractally rough particles studied by scattering. Phys Rev B 1989;39:9742–5.
[19] Patra AK, Ramanathan S, Sen D, Mazumder S. SANS study of fractal microstructure and pore morphology in porous titania. J Alloys Compd 2005;397:300–5.
[20] Mazumder S, Sen D, Roy SK, Hainbuchner M, Baron M, Rauch H. Manifestation of the statistical nature of a medium in multiple small-angle scattering. J Phys: Condens Matter 2001;13:5089–102.
[21] Sabine TM, Bertram WK. The use of multiple-scattering data to enhance small-angle neutron scattering experiments. Acta Crystallogr, A 1999;55:500–7.
[22] Knudsen KD, Fossum JO, Helgesen G, Haakestad MW. Small-angle neutron scattering from a nano-layered synthetic silicate. Phys B: Condens Matter 2004;352:247–58.
[23] Radliński AP, Boreham CJ, Lindner P, Randl O, Wignall GD, Hinde A, et al. Small angle neutron scattering signature of oil generation in artificially and naturally matured hydrocarbon source rocks. Org Geochem 2000;31:1–14.
[24] Beurroies I, Duffours L, Delord P, Woignier T, Phalippou J. Fractal geometry change induced by compression densification. J Non-Cryst Solids 1998;241:38–44.
[25] László K, Bóta A, Nagy LG, Subklew G, Schwuger MJ. Fractal approach of activated carbons from solid waste materials. Colloids Surf, A 1998;138:29–37.
[26] Hinde AL. PRINSAS – a windows-based computer program for the processing and interpretation of small-angle scattering data tailored to the analysis of sedimentary rocks. J Appl Crystallogr 2004;37:1020–4.
[27] Wong P, Bray AJ. Porod scattering from fractal surfaces. Phys Rev Lett 1988;60:1344.

[28] Leng Y, Gu J, Cao W, Zhang T-Y. Influences of density and flake size on the mechanical properties of flexible graphite. Carbon 1998;36:875–81.
[29] Cosculluela A, Farre J. Uniaxial compressive behaviour of an isotropic graphite. J Phys IV 1997;07:471–6.
[30] Meyer C, Asnacios S, Kléman M. Universal properties of lamellar systems under weak shear. Eur Phys J E 2001;6:245–53.
[31] Berto F, Lazzarin P, Ayatollahi MR. Brittle fracture of sharp and blunt V-notches in isostatic graphite under torsion loading. Carbon 2012;50:1942–52.
[32] Horn AJ, Sherry AH. Prediction of cleavage fracture from non-sharp defects using the Weibull stress based toughness scaling model. Int J Press Vessels Pip 2010;87:670–80.